

Research Article

A Novel Approach to Evaluate the Benefits of Casing Treatment in Axial Compressors

Guillaume Legras,¹ Isabelle Trébinjac,¹ Nicolas Gourdain,²
Xavier Ottavy,¹ and Lionel Castillon³

¹LMFA, UMR 5509, Ecole Centrale de Lyon, UCB Lyon I and INSA, 69134 Ecully, France

²CERFACS, Computational Fluid Dynamics Team, 42 Avenue Gaspard Coriolis, 31057 Toulouse, France

³ONERA, Applied Aerodynamics Department, 8 Rue des Vertugadins, 92190 Meudon, France

Correspondence should be addressed to Guillaume Legras, guillaume.legras@gmail.com

Received 13 December 2011; Accepted 3 April 2012

Academic Editor: Cheng Xu

Copyright © 2012 Guillaume Legras et al. This is an open access article distributed under the Creative Commons Attribution License, which permits unrestricted use, distribution, and reproduction in any medium, provided the original work is properly cited.

Passive control devices based on casing treatments have already shown their capability to improve the flow stability in axial compressors. However, their optimization remains complex due to a partial understanding of the related physical mechanisms. In order to quantitatively assess the interaction between slots and the blade tip flow, the present paper develops a novel analysis methodology based on a control-volume approach located in the rotor tip region. This methodology may be used for analyzing the casing treatment based on both axi- and non-axisymmetric slots design. The second issue of the paper focuses on the application of the current approach to better understand the effects of axi- and non-axisymmetric grooves in three different axial compressors which differ by the flow regime (subsonic/transonic) and the smooth casing shape (cylindrical/concave). Numerical simulations are performed, and results of the current approach with and without casing treatments are compared.

1. Introduction

Today, it is mandatory for compressor designers to improve performance in terms of efficiency and operating range characterized by the stall margin at low mass flow rate. One of the main difficulties encountered in this process is that compressor stall is not always controlled through normal aerodynamic design. Thus stall prevention techniques must be used, and one promising technology known to bring substantial stability for tip critical compressor rotor is casing treatment (CT) [1]. This passive control device consists of slots within the rotor casing and presents various types of geometries: circumferential grooves [2–9], non-axisymmetric slot-type CT [10–14] and self-recirculating flow channels [15–17], and honeycomb [18]. Hathaway [19] provides an extensive overview of the research studies over the last 50 years that attempt to uncover the physics behind the improvement in stall margin.

However, this understanding is still not complete since experimental measurements in the near casing region are elaborate. Moreover, postprocessing numerical results using

2D or 3D views hardly allow a quantification and can cause in some cases a misunderstanding of the flow mechanisms. Therefore, CT design requires analysis methods that need to be as easy as possible to handle for aeroengine designers. In this context, Shabbir and Adamczyk [3] proposed an approach based on a budget analysis of the steady axial momentum equation close to the rotor casing. This methodology provides further insight into the flow mechanisms relevant to compressor stability systems. In fact, their paper shows the approach is innovative to quantitatively ascertain the influence of a design on the near casing flow and provides guidance on groove design along the axial direction. However, the Shabbir and Adamczyk methodology is restrained to the knowledge of changes in the balance of the steady axial momentum equation while CT interaction with the main flow is strongly complex (tridimensional and unsteady), thus requiring information coming from each of the Navier Stokes equations.

The current paper aims at further understanding and quantitatively diagnosing complex flow mechanisms such as those induced by CT. First, the paper described an extended

Shabbir and Adamczyk model (ESA model) that calculates the budget analysis of the Navier-Stokes set of (un)steady equations. Then, the model is used to investigate the flow mechanisms induced by CT in three different axial compressors. The idea is here to have a large test range in order to study the correlation between CT and the flow regime (subsonic and transonic), CT and the original smooth wall (SW) geometry (cylindrical or conical), and finally the main difference between axi- and non-axisymmetric CT. Results are based on numerical 3D calculations. In order to apprehend this novel approach, the control-volume analysis is hereafter limited to the axial momentum equation.

2. Flow Analysis Methodology

2.1. Equations. A control volume fixed in time and located in the near casing flow is retained. This will provide a quantitative understanding of the relevant fluid mechanisms associated with SW and CT configurations. Thus, the balance between the various terms which appear in the Navier-Stokes equations is analyzed based on its finite volume formulation. For simplicity reasons, the equations are considered in the relative rotor frame and in cylindrical coordinates. Using the divergence theorem, the Navier-Stokes equations in integral form can be written as follows:

$$V \int_{\partial t} \frac{\partial \mathbf{Q}}{\partial t} = - \oint_{\partial \Omega} [\mathbf{B} dA_r + \mathbf{C} dA_\theta + \mathbf{D} dA_z] + VT, \quad (1)$$

where A_r , A_θ , and A_z are the projection areas of the control volume, V the constant volume of the control domain, \mathbf{Q} the conservative variables, \mathbf{B} , \mathbf{C} , and \mathbf{D} vectors resulting from the development of the advective and diffusive fluxes, and \mathbf{T} the forces per unit volume (usually named source terms). These vectors are recalled in (2). The stresses in (2) include both viscous and Reynolds stresses. In the same manner, the heat flux takes into account the heat flux and the enthalpy turbulent diffusion flux. This last term and the Reynolds stresses are both approximated by an eddy viscosity model:

$$\mathbf{Q} = \begin{bmatrix} \rho \\ \rho W_r \\ \rho W_\theta \\ \rho W_z \\ \rho E_r \end{bmatrix},$$

$$\mathbf{B} = \begin{bmatrix} \rho W_r \\ (\rho W_r^2 + P_s) - \tau_{rr} \\ \rho W_\theta W_r - \tau_{r\theta} \\ \rho W_z W_r - \tau_{rz} \\ (\rho E_r + P_s - \tau_{rr}) W_r - (W_\theta \tau_{r\theta} + W_z \tau_{rz} + q_r) \end{bmatrix},$$

$$\mathbf{C} = \begin{bmatrix} \rho W_\theta \\ \rho W_r W_\theta - \tau_{r\theta} \\ (\rho W_\theta^2 + P_s) - \tau_{\theta\theta} \\ \rho W_z W_\theta - \tau_{z\theta} \\ (\rho E_r + P_s - \tau_{\theta\theta}) W_\theta - (W_r \tau_{r\theta} + W_z \tau_{z\theta} + q_\theta) \end{bmatrix},$$

$$\mathbf{D} = \begin{bmatrix} \rho W_z \\ \rho W_r W_z - \tau_{rz} \\ \rho W_\theta W_z - \tau_{\theta z} \\ (\rho W_z^2 + P_s) - \tau_{zz} \\ (\rho E_r + P_s - \tau_{zz}) W_z - (W_r \tau_{zr} + W_\theta \tau_{z\theta} + q_z) \end{bmatrix},$$

$$\mathbf{T} = \begin{bmatrix} 0 \\ \frac{\rho W_\theta^2 - P_s - \tau_{\theta\theta}}{r} + 2\rho\omega W_\theta + \rho\omega^2 r \\ \frac{\rho W_\theta W_r - \tau_{r\theta}}{r} - 2\rho\omega W_r \\ 0 \\ \rho\omega^2 r W_\theta \end{bmatrix}. \quad (2)$$

2.2. Numerical Resolution. Since the objective is to understand the balance of the various terms using numerical CFD results, the semidiscretised in space for uncoupled time/space integration formulation of (1) is considered. This procedure corresponds to the finite volume method. For an individual basic hexahedral cell, this formulation is written as follows:

$$\frac{\partial \mathbf{Q}}{\partial t} = -\frac{1}{V} \left[\sum_{l=1}^6 \mathbf{F} \cdot \mathbf{N}_{\Sigma_l} - VT \right] = -\frac{1}{V} \mathbf{R}(\mathbf{Q}), \quad (3)$$

where l designates the l th face bounding the cell, \mathbf{F} the numerical approximation of the exact flux (including the below tensors \mathbf{B} , \mathbf{C} , and \mathbf{D}), \mathbf{N}_{Σ_l} the external (nonunit) normal to the face $\Sigma_l = [A_{rl}, A_{\theta l}, A_{zl}]^T$, and \mathbf{R} the numerical modelling residual of variable \mathbf{Q} .

In order to access the information of all individual terms, a computation postprocessing tool has been developed. Since the volume does not depend on time, the source terms \mathbf{T} can be directly determined using (2). Concerning the time derivative terms, the choice is done to determine those terms at instant n by computing the opposite of the numerical modelling residual at the same instant:

$$V \frac{\partial \mathbf{Q}_n}{\partial t} = -\mathbf{R}(\mathbf{Q}_n). \quad (4)$$

Therefore, only the convective fluxes have to be computed (here with a 2nd-order centered Jameson scheme [21]).

Since most CFD codes solve the Navier-Stokes equations in the cartesian reference frame, a specific treatment was done to recover terms of (2) in cylindrical coordinates. To do so, the fluxes constitutive of terms in (2) are build up through projections of the cartesian fluxes into the cylindrical reference frame. This strategy, instead of applying a cylindrical spatial scheme, permits to ensure the same numerical modelling residual than that in the cartesian equations. Equation (5) presents the transformation matrix P for rotation by an angle of θ over the longitudinal direction (i.e., z). Equation (6) recalls the expressions for projections from cartesian to cylindrical coordinates of the face areas \mathbf{A} , the relative

velocity vector \mathbf{W} , the stress tensor τ , and the heat flux vector \mathbf{q} :

$$P = \begin{bmatrix} \cos \theta & -\sin \theta & 0 \\ \sin \theta & \cos \theta & 0 \\ 0 & 0 & 1 \end{bmatrix} \quad (5)$$

$$\begin{aligned} \mathbf{A}_{r\theta z} &= P^{-T} \cdot \mathbf{A}_{xyz}, & \mathbf{W}_{r\theta z} &= P^{-T} \cdot \mathbf{W}_{xyz}, \\ \boldsymbol{\tau}_{r\theta z} &= P^{-T} \cdot \boldsymbol{\tau}_{xyz} \cdot P, & \mathbf{q}_{r\theta z} &= P^{-T} \cdot \mathbf{q}_{xyz}. \end{aligned} \quad (6)$$

For sake of clarity, the nomenclature used by Shabbir and Adamczyk [3] is chosen. The operator $\Delta(\cdot) = \sum_{l=1}^6 (\cdot)$ is introduced and characterizes the balance of flux on an individual basic cell. For example, the term $\Delta(\rho W_z W_r A_r)$ appearing in the axial momentum equation corresponds to the transport of the axial momentum across the radial faces of a basic grid cell.

The objective is to understand the balance of the various terms by using data on a mesh grid. Thus, it is obvious that the control volume retained is based on this mesh. In consequence, the current approach is extended to a control volume composed of multiple grid cells. The operator $\sum_r \sum_\theta \sum_z (\cdot) = \sum_{r,\theta,z} (\cdot)$ is introduced and realizes the cumulative sum on each individual grid cell. For example, the unsteady axial momentum equation can be written as follows:

$$\begin{aligned} \sum_{r,\theta,z} \Delta(\rho W_z W_r A_r) + \sum_{r,\theta,z} \Delta(\rho W_z W_\theta A_\theta) + \sum_{r,\theta,z} \Delta(\rho W_z^2 A_z) \\ + \sum_{r,\theta,z} \Delta(P_s A_z) + \sum_{r,\theta,z} (F_{\lambda_2}) + \sum_{r,\theta,z} (F_{\lambda_4}) - \sum_{r,\theta,z} \Delta(\tau_{rz} A_r) \\ - \sum_{r,\theta,z} \Delta(\tau_{\theta z} A_\theta) - \sum_{r,\theta,z} \Delta(\tau_{zz} A_z) \\ = R(\rho W_z) = V \frac{\partial \rho W_z}{\partial t}, \end{aligned} \quad (7)$$

where F_{λ_2} and F_{λ_4} correspond, respectively, to the 2nd and 4th numerical scalar artificial dissipation fluxes. These have been added to the equation due to the use of the 2nd-order centered Jameson scheme [21] in the numerical simulations. Therefore, the novel method allows the quantification of artificial dissipation fluxes on the balance of the axial momentum equation. Moreover, it is possible to localize regions and flow structures where these fluxes are active. Finally, notice that each term of (7) is homogeneous to a force per unit volume ($[\text{kg} \cdot \text{m}^{-2} \cdot \text{s}^{-1}]$).

2.3. Application of the ESA Model

2.3.1. On Steady Flows. In the case of steady flow problems, time derivative terms are null leading to a balance of the advective and viscous fluxes and forces per volume unit. In practice, the precision of this equilibrium depends on the value of the numerical residual \mathbf{R} . For numerical data, it tends to reach zero at convergence according to the machines' precision. Equation (3) can be simplified as follows:

$$\mathbf{R}(\mathbf{Q}) \approx 0 \iff \sum_{i=1}^6 \mathbf{F} \cdot \mathbf{N}_{\Sigma_i} - VT_\Omega \approx 0. \quad (8)$$

2.3.2. On Unsteady Flows. Concerning unsteady flow problems, time derivative terms need to be determined since they can strongly impact the equilibrium of the equations. Those are taken equal to $-\mathbf{R}(\mathbf{Q})$, which is consistent only if the result analyzed is a time-consistent solution (usually a periodic solution).

The current approach can be applied both on unsteady and time-averaged solution allowing access of specific information of the numerical modelling residual. In fact, assuming that any flow variable \mathbf{Q} can be decomposed into its mean term $\bar{\mathbf{Q}}$ plus its deterministic component \mathbf{Q}' (stochastic component \mathbf{Q}'' is neglected), that is, $\mathbf{Q} = \bar{\mathbf{Q}} + \mathbf{Q}'$, and by replacing each variable in (3), the residual operator can be written as

$$\overline{\mathbf{R}(\mathbf{Q})} = \mathbf{R}(\bar{\mathbf{Q}}) + \overline{\mathbf{R}(\mathbf{Q}') = 0}, \quad (9)$$

where $\overline{\mathbf{R}(\mathbf{Q})}$ denotes the time-averaged balance of equation and tends to zero since the unsteady problem is periodic in time. $\mathbf{R}(\bar{\mathbf{Q}})$ designates the residual applied to the time-averaged flow field. $\mathbf{R}(\mathbf{Q}')$ indicates the time-averaged effect of the unsteadiness (also called lumped deterministic source terms by Ratzlaff et al. [23]).

3. Description of the Investigated Axial Compressors

In order to understand the CT effects on axial compressors features, three axial compressors are numerically investigated with and without CT: NASA Rotor 37 [24, 25], CREATE [26], and CBUAA [22, 27]. They differ by the geometry of the smooth casing (cylindrical versus noncylindrical), the flow regime (subsonic versus transonic), and the CT geometry incorporated (circumferential grooves or slot-type CT). These differences are resumed in Table 1. The following paragraphs further describe the design features of these three compressors.

3.1. NASA Rotor 37. The well-known transonic experimental compressor NASA Rotor 37 (Figure 1) was designed and tested at the NASA Lewis Research Center [24, 25]. The main characteristics are recalled in Table 2. More details about the compressor design, extensive results, and comparisons of numerical and experimental data may be found in the following references: Suder and Celestina [28], Chima [29], Denton [30], and Dunham [20]. The NASA Rotor 37 has been chosen since it is known for the occurrence of the blade tip located rotating stall phenomena at operating close to surge [31]. Note that the original configuration experimentally tested does not include any CT (i.e., experimental data are only available for the SW configuration). The implementation of casing grooves is only investigated through numerical simulations.

The CT geometry is taken from Legras et al. [8] and consists of 6 circumferential slots (Figure 5(a)). Each groove is 3 mm wide (10.9% of rotor tip axial chord) with a gap of 1.5 mm between each cavity. The height-to-width ratio is 0.7 : 1. The first groove starts at around $x/C = 5\%$ of the tip chord upstream of the rotor tip leading edge. Concerning the

TABLE 1: Differences between the axial compressors investigated.

		Investigated compressors		
		NASA Rotor 37	CREATE S1-R2	CBUAA
Geometry of the casing	Cylindrical	—	X	X
	Noncylindrical	X	—	—
Geometry of CT	Circumferential	X	X	—
	Slot type	—	—	X
Type of regime	Subsonic	—	X	—
	Transonic	X	—	X

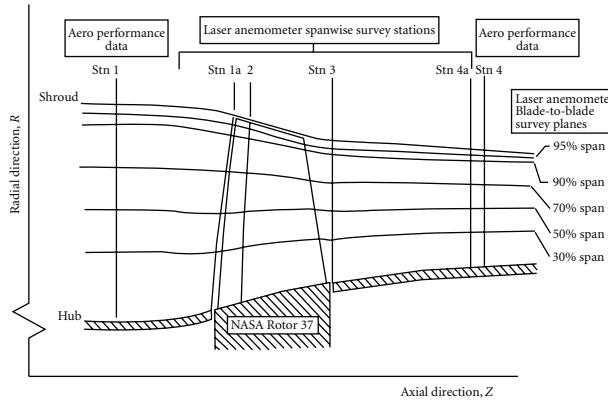


FIGURE 1: Cross-section of the NASA Rotor 37 [28].

TABLE 2: Design features of the NASA Rotor 37 [20].

Number of blades	36
Tip radius at leading edge	252 mm
Aspect ratio	1.19
Hub-tip radius ratio	0.70
Tip solidity	1.288
Tip clearance height	0.356 mm
Rotation speed	17188.7 rpm
Tip speed	457 m/s
Total pressure ratio	2.106
Adiabatic efficiency	0.877
Design mass flow	$20.188 \text{ kg} \cdot \text{s}^{-1}$
Choked mass flow	$20.93 \pm 0.14 \text{ kg} \cdot \text{s}^{-1}$

design, the objective was not to optimize the CT geometry but to reach a comprehensive description of the change in flow properties generated by the grooves. Therefore, it was found interesting to investigate the impact of a slot that surmounts the blade tip leading edge, even if its usefulness is not obvious.

3.2. Multistage Compressor CREATE. CREATE (Compresseur de Recherche pour l'Etude des Effets Aérodynamiques et Technologiques, Figure 2) is a research 3.5-stage axial compressor designed by SNECMA and tested at the Ecole Centrale de Lyon in LMFA research laboratory. This subsonic compressor is dedicated to aerothermal and aerodynamic

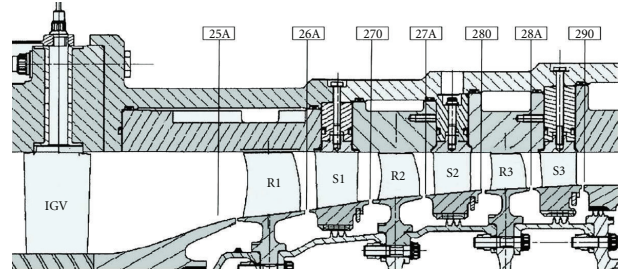


FIGURE 2: Cross-section of the CREATE high-pressure compressor and measurement planes.

TABLE 3: Design features of CREATE.

Cylindrical outer casing diameter	0.52 m
Rotation speed	11543 rpm
Tip rotor speed	$313 \text{ m} \cdot \text{s}^{-1}$

TABLE 4: Number of blades of CREATE rows.

Row	IGV	R1	S1	R2	S2	R3	S3
Number of blades per row (for 2π)	32	64	96	80	112	80	128
Number of blades for $2\pi/16$	2	4	6	5	7	5	8

studies. Its geometry and rotation speed are representative of high-pressure compressor median-rear blocks of modern turbojet engine. Its design features are recalled in Tables 3 and 4. More details about the compressor design can be found in Touyeras and Villain [26]. Thanks to the large amount of measurements, this experimental compressor has been the subject of different research works focused on rotor/stator interactions [32, 33] and CFD methods calibration and improvement [34–36].

It was numerically seen at nominal speed that the stability of the untreated casing compressor is limited by the tip clearance effects on stages 2 and 3 [36]. As a result, it was chosen to implement on both stages a CT in the form of five axisymmetric grooves of equal width and equally distributed in the axial direction. Details of the design study can be found in Perrot et al. [4]. Note that, for confidentiality reasons, slots dimensions are not mentioned, and the following results are normalized. However, for the purpose of the current study, the CT flow analysis is only focused on the grooves implemented in the R2 rotor row. Furthermore, notice that the numerical results are based on Legras et al. [37].

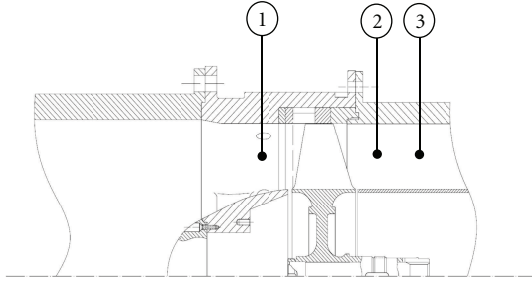


FIGURE 3: Cross-section view of the test section [22].

TABLE 5: Design features of the CBUAA [22].

Blade number	17
Tip diameter	355.8 mm
Design speed	22000 rpm
Hub-to-tip ratio	0.565
Aspect ratio	0.956
Mass flow at design point	13.4 kg·s ⁻¹
Total pressure ratio at design speed	1.6 (stage)
Adiabatic efficiency at design speed	0.88 (stage)
Relative Mach number of tip rotor speed	1.404

Performances are obtained on the overall configuration R1-S3, whereas the CTs implemented in R2 are investigated using modelisation of the S1-R2 configuration.

3.3. CBUAA Compressor Test Case. The Compressor of the Beijing University of Aeronautics & Astronautics (CBUAA) is a single-stage transonic axial compressor (Figure 3). A brief description of the test rotor can be seen in Table 5. In the experiment, the stator is placed far downstream of test rotor; thus the isolated rotor environment can be established. Experimental and numerical studies of the test case can be found in Lin et al. [22] and Ning and Xu [27].

The slot-type CT is illustrated in Figure 4 [22, 27]. The total slot number is 153 (9 times the blade number). The slots are skewed to have a 45 degrees angle so that their openings face the pressure side of the blades. The axial length of the slots is 79% of the blade tip axial chord (with 39% exposed to the blade tip). The ratio of the open area of the slots to the casing annulus area is 0.8. The radial depth of the slots is 9 mm. Moreover, the CT has a recess chamber and its radial depth is 9 mm.

4. Compressors Modelisation

4.1. Description of the Numerical Methods. All numerical simulations are carried out using the *elsA* software developed by ONERA and CERFACS [38]. The code solves the Favre-Reynolds-averaged Navier-Stokes equations on multi-block structured meshes using a cell-centered finite-volume approach. It also allows the use of the Chimera method dedicated to modelize complex geometries typically generated by technological effects [39]. Thus, the Chimera method is here used to model the CT.

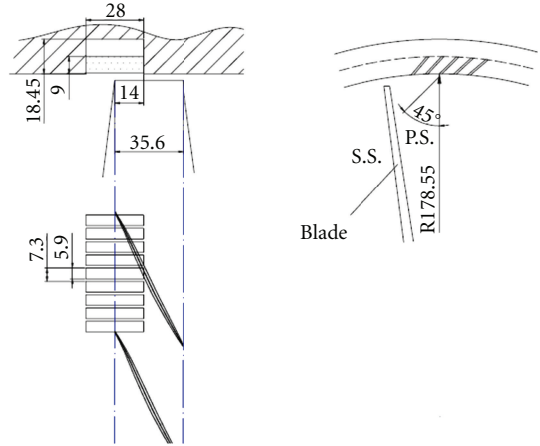


FIGURE 4: Sketch of the CBUAA slot-type casing treatment [22].

Computations were run with a 2nd-order centered Jameson scheme [21] for the estimation of convective fluxes. The time marching is performed by an efficient implicit time integration scheme based on the backward Euler scheme and a scalar lower-upper (lu) symmetric successive overrelaxation (SSOR) method. Concerning the numerical approach, it differs depending on the investigated compressor case (see Table 6).

For the NASA Rotor 37 configuration, circumferential grooves are axisymmetric. They can be considered as a continuing circumferential modification of the casing and then be computed similarly to SW configuration in a conventional steady-state approach.

Concerning the CREATE S1-R2 configuration, the use of an unsteady approach with phase-lagged boundary conditions at the rows' interfaces and on the periodic boundaries enables to consider only one single-blade passage for each row [40, 41].

For CBUAA case with slot-type CT, simulations used an unsteady overset grids' method coupled with a phase-lagged condition at the interface between rotor and CT slot Chimera blocks [42]. This procedure reduces the computational domain to one single-blade passage and one CT slot.

The turbulence is modelized by the two-equation model $k - \omega$ proposed by Wilcox [43] for both the NASA Rotor 37 and the CBUAA, and the two-equation model of $k - \varepsilon$ low-Reynolds of Launder-Sharma for the CREATE case. The flow is assumed to be fully turbulent since the mean Reynolds number based on the blade chord is approximately 5.10^6 .

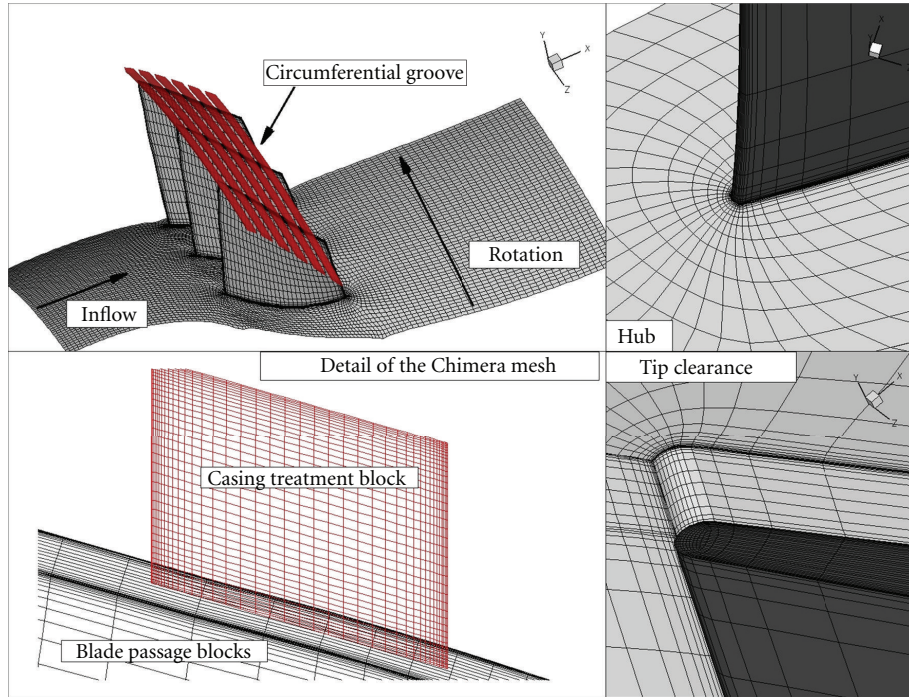
Numerical validation and other modelling details are given, respectively, for

- (i) the NASA Rotor 37 in Legras et al. [8, 9],
- (ii) the CREATE case in Legras et al. [37],
- (iii) the CBUAA in Legras et al. [44], Castillon and Legras [42].

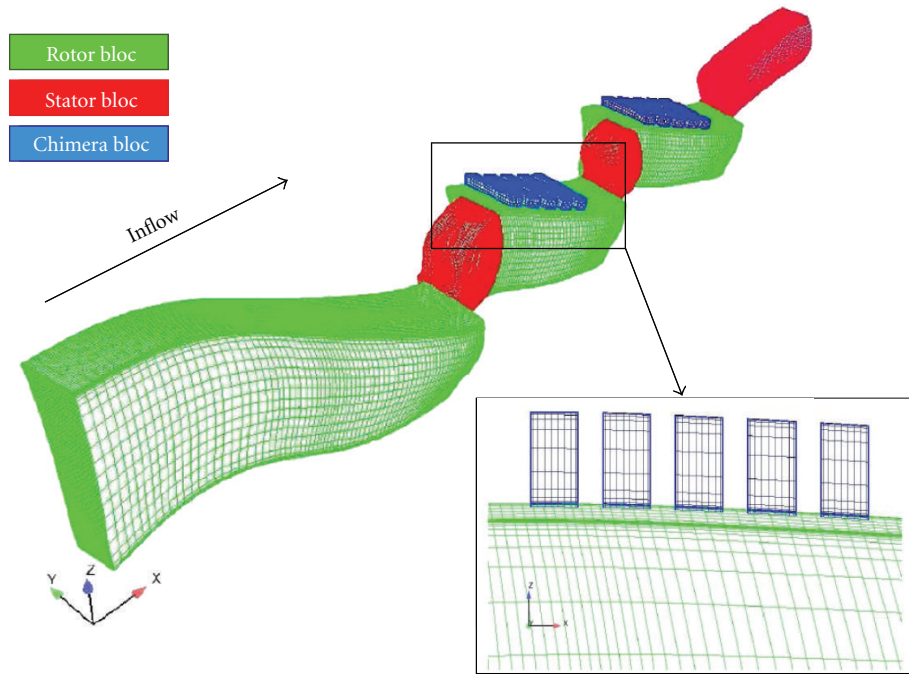
4.2. Meshing Strategies. For all compressors, the flow domain is discretized with a low-Reynolds multiblock structured

TABLE 6: Numerical approaches performed according to the compressor investigated.

Numerical approaches	Investigated compressors		
	NASA Rotor 37 axi. CT	CREATE S1-R2 axi. CT	CBUAA non axi. CT
Steady	X	—	—
Unsteady (phase-lagged)	—	X	X



(a) NASA Rotor 37



(b) CREATE

FIGURE 5: Chimera meshes used for modelling circumferential CT.

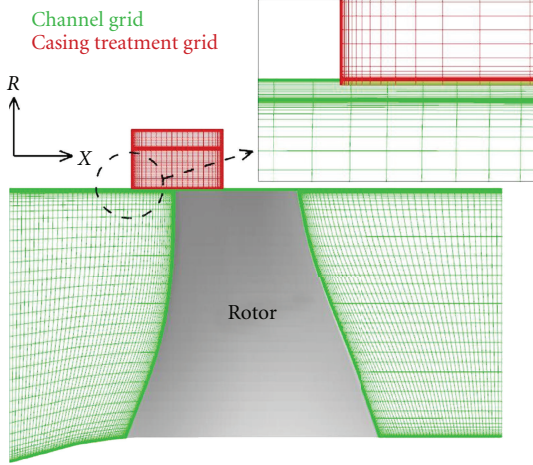


FIGURE 6: Chimera mesh used for modelling the slot-type CT of the CBUAA case.

approach. Each SW configuration counts approximately a total of 1.2–1.5 million grid points. The meshes are clustered towards the solid boundaries in order to reach the resolution requirement of $y^+ \approx 1$ (the size of the first layer is approximatively $1\mu\text{m}$). They are characterized by 89 grid points in the spanwise direction. The tip leakage region is discretized using a “O-H” grid topology with 25 points in the radial direction.

Concerning the CT configurations, they are based on the SW meshes at which “H” Chimera blocks modelling the casing grooves have been added (Figures 5 and 6).

5. Overall Performances

Figures 7, 8, and 9 present the measured and calculated performances at design speed, respectively, for the NASA Rotor 37, CREATE R1-S3 configuration, and CBUAA.

5.1. Results of the NASA Rotor 37. In Figure 7, the mass flow rates are normalized by the experimental choked mass flow ($20.93\text{ kg}\cdot\text{s}^{-1}$). The pressure ratio-mass flow curves show a fairly good agreement between numerical and experimental results for the SW configuration. However, the efficiency curve resulting from the simulation is clearly shifted which leads to underestimate the efficiency whatever the mass flow.

The numerical results of the CT configuration show only slight differences with the SW case in terms of performance (Figure 7). As observed by Legras et al. [8, 9], those small differences are all the more surprising that important radial flow exchanges occur between the 2nd and the 4th slots and the main flow. It is interesting to note that nearly all numerical studies that investigate CT for the NASA Rotor 37 present a relative insensitivity of the slots on the performance (circumferential grooves [45–47]; semicircular slots [31]). The application of the current methodology applied on the near casing flow region can be useful to ascertain the flow mechanisms, to quantify the fluxes and finally to understand

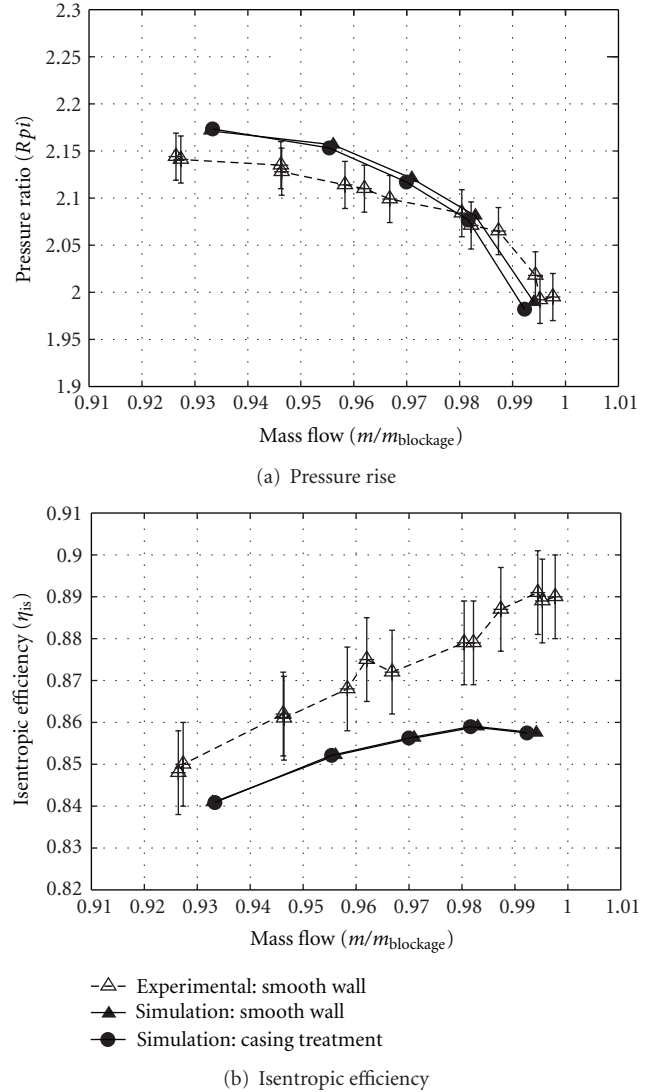


FIGURE 7: Predicted NASA Rotor 37 characteristics at design speed.

why the implementation of CT is nonefficient in the NASA Rotor 37.

5.2. Results of the CREATE R1-S3 Configuration. Overall performances presented in Figure 8 are normalized by the SW values at nominal operating conditions. Experimental uncertainties are 0.46%, 0.17%, and 0.32%, respectively, for the mass flow rate, the pressure ratio, and the isentropic efficiency. Concerning the steady numerical results, the limit of stability is estimated considering the last converged calculation.

Results in Figure 8 show that the shapes of the pressure rise and isentropic efficiency curves are correctly represented by the simulations. The main information of Figure 8 is that the numerical simulation is able to predict the trend observed in the measurement that CT improves performances compared to the SW case. The relative shifts in performance between both cases at design operating condition speed are

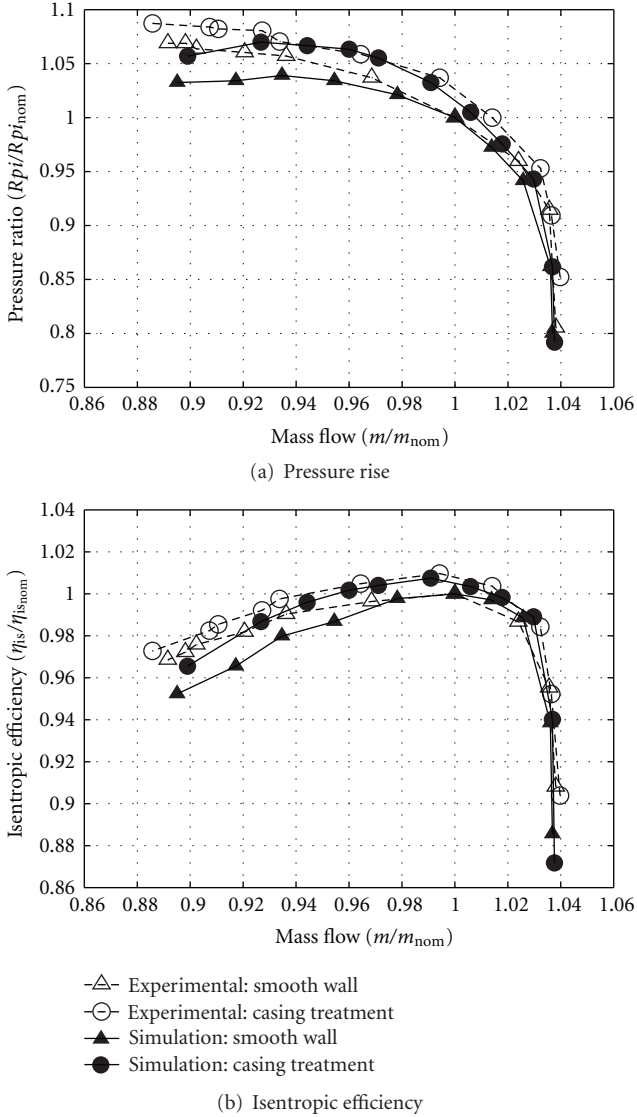


FIGURE 8: CREATE characteristics relative to nominal operating point (experimental versus numerical simulations).

approximately $\Delta\eta_{is,max} = +1\%$, $\Delta Rpi_{max} = +2\%$. For the steady simulations of the whole compressor being validated, let us analyze the unsteady calculations of the S1-R2 configuration.

Moreover, Legras et al. [37] present local flow comparisons between CFD results and LDA measurements done in the rotor tip clearance and inside the CT of CREATE compressor. They proved that the CFD model correctly predicts the main characteristics of the flow in this region and particularly the rotor tip vortex, the flow inside the CT, and the flow interactions between the CT and the throughflow (i.e., radial flow exchanges).

5.3. Results of the CBUAA. Rotor characteristics of both SW and CT configurations obtained at 98% speed by the experiment [22] and predicted by unsteady simulations are

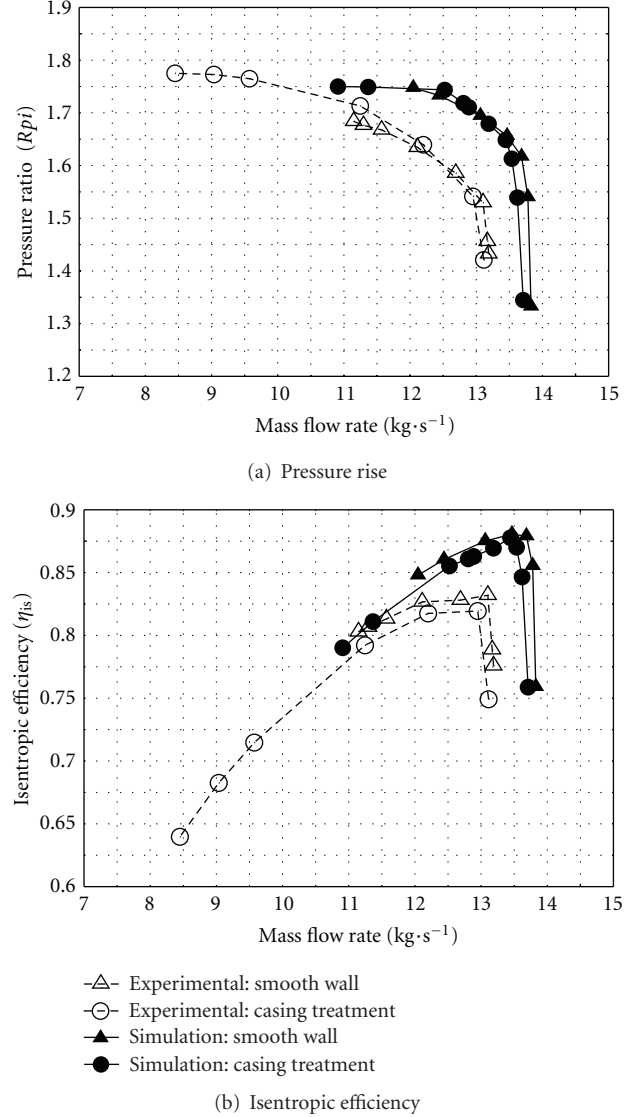


FIGURE 9: CBUAA characteristics at design speed (experimental versus numerical simulations).

compared in Figure 9. The numerical curves shapes are in fairly good agreement with the measurements. However, numerical characteristics are shifted due to a larger mass flow rate at choked conditions than the measured value (as predicted by Lin et al. [22] and Ning and Xu [27]). Simulations overestimate total pressure as well as efficiency magnitudes. The stable operating range of the SW configuration is correctly predicted. Concerning CT case, simulations clearly underestimate the operating range due to the onset of stall point at higher mass flow rate than the experiment. Finally, the calculated efficiency curves of the CT configuration show lower magnitude than the SW case one in the SW operating range, whereas the magnitude of the total pressure CT curve is similar. These differences have also been observed by other authors who numerically investigated the present test case [22, 27].

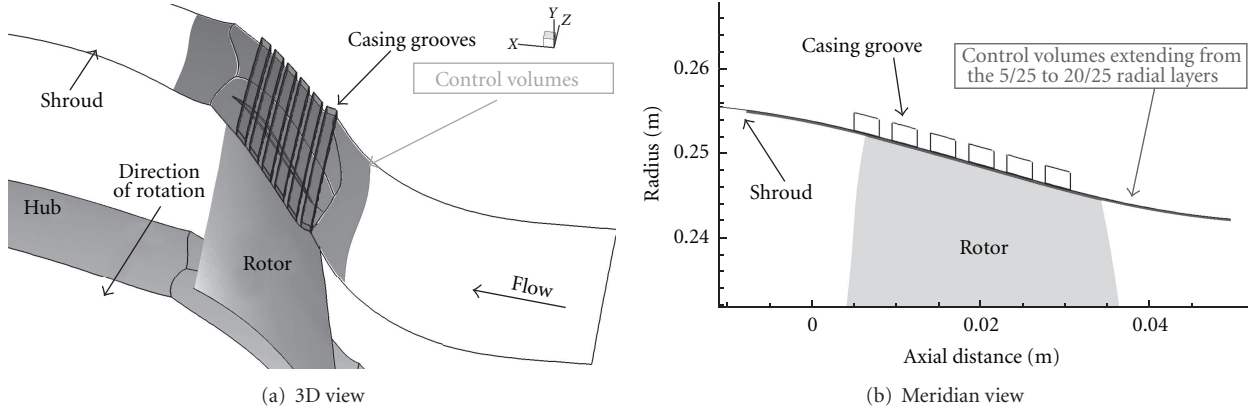


FIGURE 10: Views of the control volume located at the NASA Rotor 37 tip clearance.

5.4. Discussion of the Effect of CT Design on Overall Performances. The comparison of the three compressors performances indicates that the implementation of axisymmetric CT induces a low stall margin improvement and no penalty in compressor efficiency. On the contrary, non-axisymmetric CT greatly improves the stall margin but reduces the compressor efficiency. This observation suggests that the more the CT is efficient to enhance stall margin, the more the compressor is subject to a decrease of its efficiency. This observation is in agreement with results observed in the literature by Hathaway [19].

Finally, based on the comparisons between experimental and numerical results, it was considered that the numerical models are able to reveal the overall flow mechanisms occurring near the outer casing. This is essential for the objective of the present work aiming at understanding the local influence of CT slots.

6. CT Flow Mechanisms Analysis according to the ESA Model

This section is dedicated to the analysis of the flow interaction between rotor and CT at the last SW stable operating point. To do so, the ESA model is used to get further insight into the understanding of the phenomenon. In practical terms, a control volume analysis is here performed on the blade tip flow and comparisons between SW and CT configurations are done.

6.1. Equation Analyzed. As it has been observed in previous studies, the CT interaction with the blade tip flow is mainly tridimensional and unsteady. In order to handle the results interpretation, the scope of the CT flow mechanisms' study is restrained to the analysis of the balance of the axial momentum (7). Thus, results in terms of axial forces acting on the blade tip flow are expected. This equation is chosen since it describes the global flow across the rotor channel, specially its pressure rise.

Here, we notice that the CFD computations presented before has been performed with steady as well as unsteady approaches. Thus, for the NASA Rotor 37, steady

axial momentum balance have been computed. On the contrary, for the CREATE and CBUAA cases, instantaneous axial momentum balances have been obtained for instants equally spread over a respective known temporal period:

- (i) for CREATE, 25 instants equally spread over one upstream stator blade S1 passing temporal period (T_{S1});
- (ii) for CBUAA, 17 instants spread over one CT slot passing temporal period (T_{CT}).

For these two last compressors, the contribution of the time derivative term $\partial \rho W_z / \partial t$ can be computed, which cannot be done for NASA Rotor 37. In order to permit comparisons between the three compressors, CREATE and CBUAA instantaneous axial momentum balances are time-averaged on their respective temporal periods. In other words, NASA steady axial momentum balance is here compared to CREATE and CBUAA time-averaged axial momentum balances.

6.2. Definition of the Control Volume. For all configurations, the control volume surrounds the rotor blade tip flow field as shown in Figure 10. It is circumferentially delimited by the rotor blade pitch, axially extended just upstream and downstream of the rotor blade tip, and radially bounded by the 5th/25 to the 20th/25 grid layers modelling the rotor tip clearance. Therefore, due to the Chimera technique in the grooved configurations, the control volume is not attached to the shroud. In fact, the two last radial layers normal to the casing are used for interpolation between grooves and the blade passage blocks. These are not taken into account in the control volume since they can mislead the Navier-Stokes equations equilibrium.

6.3. Global Flow Mechanisms Acting on the Near Casing Flow. Results of the axial momentum balance for the SW and CT configurations are presented, respectively, for NASA Rotor 37 in Figure 11, CREATE in Figure 12, and CBUAA in Figure 13. This kind of representation, as histograms, provides a macroscopic view of the different axial forces acting on the control volumes (i.e., the near casing flow). As a consequence, one

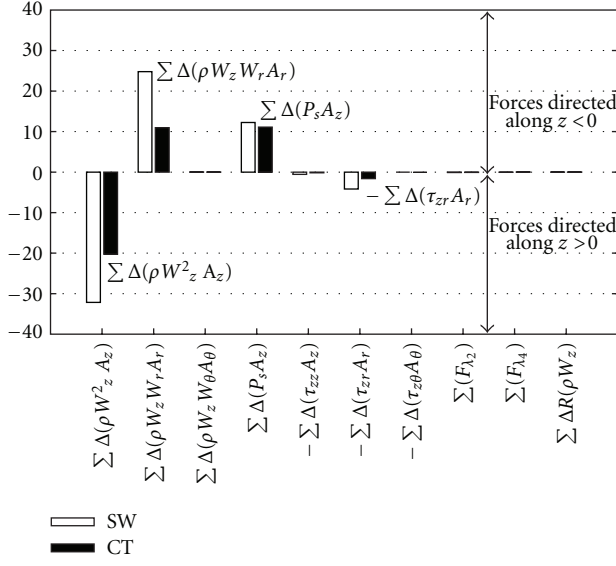


FIGURE 11: NASA Rotor 37 with and without CT: balance of the axial momentum equation.

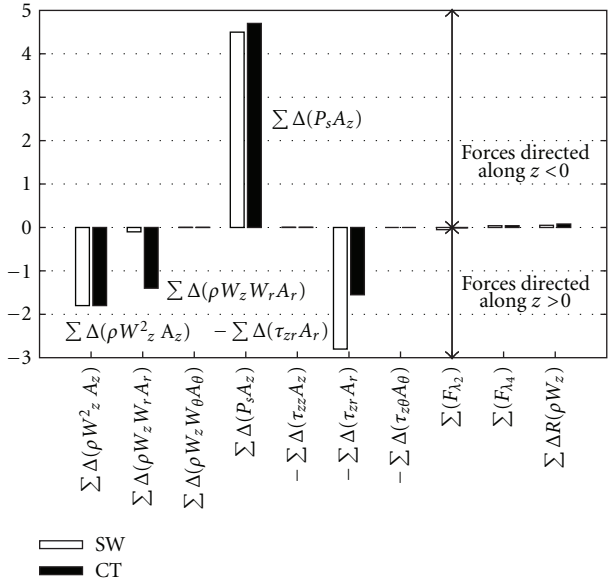


FIGURE 12: CREATE-R2 with and without CT: balance of the axial momentum equation.

has to take care of the results interpretation since histograms do not describe the local influence of CT. This will be further done in the next section titled “Longitudinal evolutions of the axial forces and CT contribution”.

Before discussing the physical analysis, it is instructive to comment on the magnitude of the numerical terms of the balance. Results show that the numerical modelling residuals $R(\rho W_z)$ tend to zero leading to a good precision of the balance of the equation. For the CREATE and CBUAA cases, it signifies that the time-averaged temporal derivative term (i.e., $= -R(\rho W_z)$) obtained from unsteady simulations

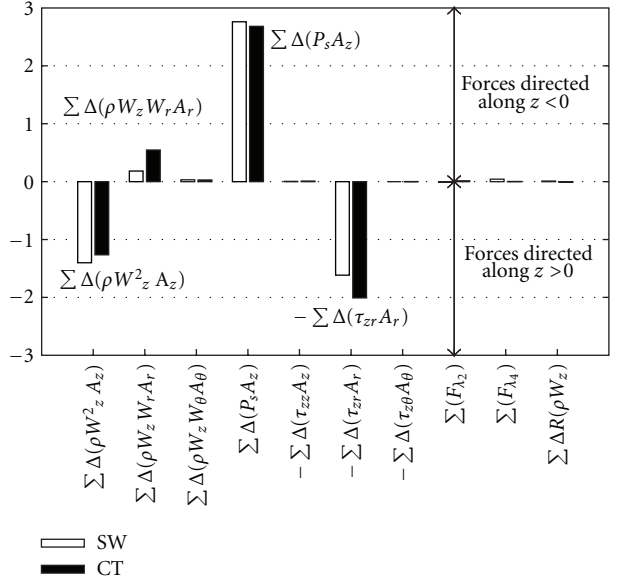


FIGURE 13: CBUAA with and without CT: balance of the axial momentum equation.

converges to zero. This observation lends support that the unsteady calculations correctly reach a time-periodic state. Moreover, it can be observed that scalar artificial viscosity fluxes (F_{λ_2} and F_{λ_4}) are insignificant in spite of the presence of a strong shock wave located in the blade tip region of the NASA Rotor 37 and the CBUAA.

6.3.1. SW Results

General Overview. For all SW configurations, results highlight the presence of four main axial forces being applied on the control volume:

- (i) the axial pressure force $\sum \Delta(P_s A_z)$ that corresponds to the axial flow pressure rise across the rotor.
- (ii) The axial force due to the transport of the axial momentum across the longitudinal faces $\sum \Delta(\rho W_z^2 A_z)$. This term is similar to a dynamic pressure force that acts on the same surfaces than the pressure force. Its value relates to the flow axial acceleration or deceleration. In fact, by simply differentiating the terms between the axial outlet and inlet of the control volume (i.e., $[(\rho W_z^2 A_z)_{\text{outlet}} - (\rho W_z^2 A_z)_{\text{inlet}}]$) and assuming that W_z is mainly positive in the volume (which is not locally true due to the presence of the tip leakage, casing boundary layer, ...), a negative (resp. positive) force corresponds to a deceleration (resp. acceleration) of the flow. The same reasoning can be done with $W_z < 0$ that leads to the inverse conclusion. Results in Figures 11, 12, and 13 indicate that the incoming flow decelerates along the axial direction. This observation is coherent with the general aerodynamic of compressor since the casing boundary layer and the tip leakage flow

- greatly influence the incoming flow. Furthermore, the term $\sum \Delta(\rho W_z^2 A_z)$ gives information on the axial flow blockage occurring in the control volume.
- (iii) The axial shear force acting on the radial faces of the control volumes $-\sum \Delta(\tau_{rz} A_r)$ induced by casing and blade tip boundary layers as well as the tip leakage flow.

- (iv) The axial force due to the transport of the axial momentum across the radial faces $\sum \Delta(\rho W_z W_r A_r)$. This term expresses the influence of the radial flow on the balance of axial forces. This force acts on the same faces than the axial shear force $-\sum \Delta(\tau_{rz} A_r)$. Thus, it is believed that a change of one of these forces can strongly influence the other.

All other terms are zero due to periodicity (forces acting on A_θ faces) or to the radial thickness of the control volume. It is worth noticing that the forces applied on the near casing flow correspond to those observed in similar works done by Shabbir and Adamczyk [3].

These axial forces can be distinguished depending on whether they are acting in the same direction of the flow ($z > 0$) or in opposite direction of the flow ($z < 0$). This information is given by the sign of the terms. A sketch describing the nomenclature of the axial forces acting on the control volume is presented in Figure 22. The results show for all compressors some coherent trends:

- (i) the axial force due to $\sum \Delta(P_s A_z)$ always acts in the opposite direction of the flow advance since the term is positive;
- (ii) the axial forces due to $\sum \Delta(\rho W_z^2 A_z)$ and $-\sum \Delta(\tau_{rz} A_r)$ always act in the same direction as the flow advance since the terms are negative.

This observation is consistent with the general aerodynamic of axial compressor. The casing boundary layer (represented by $-\sum \Delta(\tau_{rz} A_r)$) and the upstream flow advance (described by $\sum \Delta(\rho W_z^2 A_z)$) balance the adverse pressure gradient ($\sum \Delta(P_s A_z)$) created by the axial compressor. If the boundary layer separates from the casing and/or if the flow advance is too low (like when the mass flow rate is too low), the pressure rise cannot be held, thus leading to an unstable operating flow condition.

The different compressors differ by the magnitude of these axial forces and the direction of the $\sum \Delta(\rho W_z W_r A_r)$.

Influence of the Casing Geometry. Figures 11, 12, and 13 clearly highlight the impact of the annulus shape (cylindrical versus conical). In fact, both CREATE and CBUAA compressors, which have a cylindrical casing, show similar results characterized by

- (i) same relative balance between $\sum \Delta(P_s A_z)$ and the opposite axial forces $\sum \Delta(\rho W_z^2 A_z)$ and $-\sum \Delta(\tau_{rz} A_r)$,
- (ii) insignificant influence of $\sum \Delta(\rho W_z W_r A_r)$.

On the contrary, the NASA Rotor 37 that has a noncylindrical casing shows the occurrence of another axial force that is

due to $\sum \Delta(\rho W_z W_r A_r)$. This force comes to contribute with the adverse pressure force $\sum \Delta(P_s A_z)$ to counteract the flow advance (i.e., $z < 0$). This result is clearly obvious since the conical casing forces the flow to have a radial velocity component $W_r < 0$. The near casing flow deflection is large enough to affect the balance of axial momentum, and it manifests itself through the axial force $\sum \Delta(\rho W_z W_r A_r)$.

Influence of the Flow Regime. The comparison between CREATE and CBUAA (Figures 12 and 13), which, respectively, works in subsonic and transonic flow regime, indicates no major difference in the axial momentum balance. Furthermore, the comparison between NASA Rotor 37 and CBUAA (Figures 11 and 13) proves that the shape of the rotor casing has a greater influence than the flow regime.

6.3.2. CT Results

General Overview. The results of the CT configurations in Figures 11, 12, and 13 show the same type of forces acting on the blade tip flow than SW cases. However, the influence of CT is here revealed by changes of the axial forces contribution.

For all compressors, the magnitude of pressure rise across the rotor $\sum \Delta(P_s A_z)$ follows the predicted overall performances (see Figures 7, 8, and 9).

Due to the radial flow exchanges between the grooves and the throughflow (see [9, 37, 44] for images of the flow exchanges), CT is expected to contribute to balance the axial momentum equation with additional terms. As previously assumed in the SW analysis, the radial flow exchanges might influence the axial momentum equation through the force $\sum \Delta(\rho W_z W_r A_r)$. In fact, results are in agreement with this hypothesis. They clearly show that the main impact of the CT, whether it is axisymmetric or not, is revealed by the changes of $\sum \Delta(\rho W_z W_r A_r)$ and the viscous force $-\sum \Delta(\tau_{rz} A_r)$ due to the casing boundary layer. As previously announced, these two forces might influence each other since they both act on the same faces of the control volume. In fact, results reveal that the axial force $\sum \Delta(\rho W_z W_r A_r)$ changes proportionally to $-\sum \Delta(\tau_{rz} A_r)$. These observations can be interpreted as follows: the radial fluid exchanges between the CT slots and the rotor channel tend to replace the casing boundary layer in its role to balance the adverse pressure gradient. This suggests that the W_r magnitude is a key point to the CT flow mechanisms. If the reasonment is pushed further, one explanation of the CT efficiency to improve the stall margin might come from its capability to perform an axial force due to the radial flow exchanges (through the axial force $\sum \Delta(\rho W_z W_r A_r)$) more robust to the adverse pressure gradient than the casing boundary layer (through the axial force $-\sum \Delta(\tau_{rz} A_r)$). Moreover, since the shear axial force can induce a loss of efficiency, the use of radial flow exchanges as an alternative to casing boundary layer effect is very interesting in order to increase the global efficiency of the compressor rotor. As a consequence, the main difference between axisymmetric and non-axisymmetric CT can be evaluated depending on the W_r evolution.

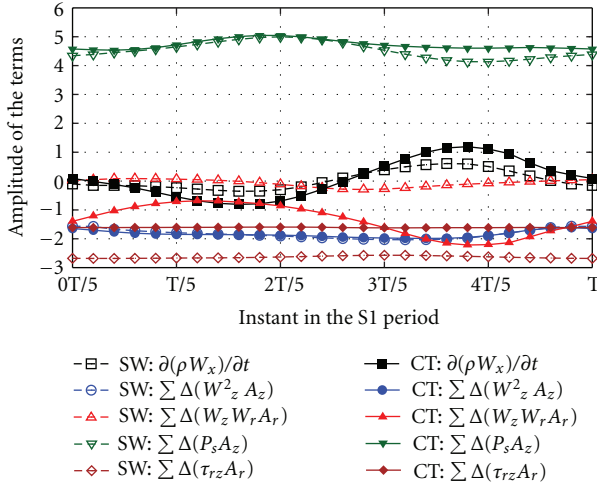


FIGURE 14: CREATE-R2 with and without CT: temporal evolution of the main terms of the unsteady axial momentum equation.

The results of the NASA Rotor 37 (Figure 11) and CREATE (Figure 12) indicate that circumferential CT contribute with additional axial force $\sum \Delta(\rho W_z W_r A_r) < 0$ acting on the flow advance. As expected, it is the effect of the radial flow exchanges and this observation is in agreement with results of Shabbir and Adamczyk [3]. This adding term $\sum \Delta(\rho W_z W_r A_r) < 0$ is accompanied with a proportional decrease of the viscous axial force $-\sum \Delta(\tau_{rz} A_r)$. It can be relied to the slight gain in efficiency observed in CREATE performances (Figure 8). As a matter of fact, the main role of axisymmetric CT is to turn or drive the force $\sum \Delta(\rho W_z W_r A_r)$ more along the main flow direction, that is, $z > 0$. This is consistent with the general conclusions that previous studies have found that the reverse tip leakage flow through the tip gap got pushed into the grooves by the re-injecting flow (in main flow direction) from the grooves.

On the contrary, the CBUAA slot-type CT contributes by additional force $\sum \Delta(\rho W_z W_r A_r) > 0$ acting in opposite direction to the flow as well as $\sum \Delta(P_s A_z)$ (Figure 13). Moreover, the viscous axial force $-\sum \Delta(\tau_{rz} A_r)$ has increased proportionally, thus explaining the slight decrease in efficiency observed in CBUAA performances (Figure 9). This first result reveals that slot-type CT behaves in a different manner than circumferential CT. However, as mentioned below histograms present a global and not a local influence of the CT. For this particular CT geometry, a local analysis has to be done to further understand the flow mechanisms as it will be seen in the next paragraphs.

For both axi- and non-axisymmetric grooves, the balance change is made possible through the modification of the radial velocity W_r induced by flow exchanges between grooves and the throughflow. It further supports that W_r is quite important for the flow stabilization in the tip region. This observation has to be confirmed by the local analysis of the CT flow mechanisms.

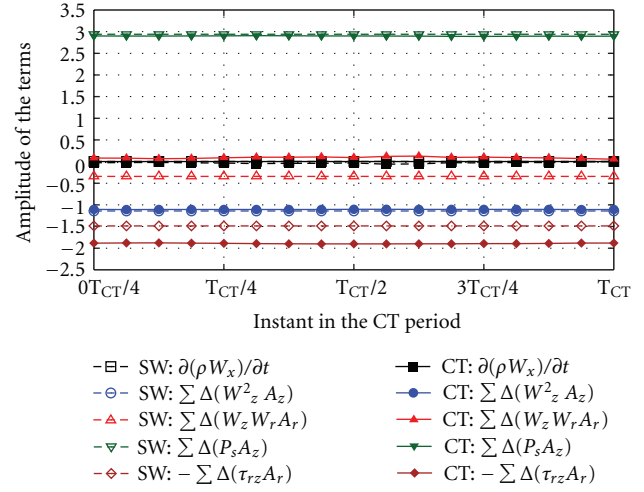


FIGURE 15: CBUAA with and without CT: temporal evolution of the main terms of the unsteady axial momentum equation.

6.3.3. Unsteady Flow Mechanisms. Figures 14 and 15 present, respectively, for CREATE and CBUAA the temporal evolution of the unsteady axial momentum balance. This analysis allows us to gain a quantitative and qualitative knowledge of the contribution of the time derivative term $\partial \rho W_z / \partial t$.

Results of the CREATE-R2. For the CREATE case, unsteady results are presented over the upstream stator S1 passing temporal period. Plots in Figure 14 show a sinusoidal time-dependent evolution of the time-derivative term influenced by the stator S1 blade passage frequency T_{S1} . Its time-averaged value tends to zero, in agreement with results shown in Figure 12. Concerning its temporal fluctuations, amplitudes are particularly pronounced for the CT case with higher values of a factor 2 compared to the SW. Moreover, results show that $\partial \rho W_z / \partial t$ amplitudes are mainly driven by those of $\sum \Delta(P_s A_z)$ in the SW case and those of $\sum \Delta(W_z W_r A_r)$ in the CT case. In fact, CT deadens the magnitude of the $\sum \Delta(P_s A_z)$ fluctuations by a factor 2 which is believed to greatly enhance the flow stability (because the pressure gradient opposes the flow). The increase in $\sum \Delta(\rho W_z W_r A_r)$ fluctuation, which drives the time-dependent term, proves that groove mechanisms strongly respond to upstream flow unsteadiness.

Results of the CBUAA. Concerning the CBUAA case, unsteady results are presented over the CT slot passing temporal period T_{CT} . Plots in Figure 15 indicate that all terms present a “quasi-steady” behaviour, supporting that unsteadiness of the CT interaction with the throughflow is insignificant. This observation is especially confirmed by the zero magnitude over T_{CT} of the time-derivative term $\partial \rho W_z / \partial t$. This “quasi-steady” behaviour has already been observed by Lin et al. [22], and Ning and Xu [27]. Indeed, the unsteady time scale of the discrete treatment slots is therefore considerably small compared to that of the blade passage [27]; thus the

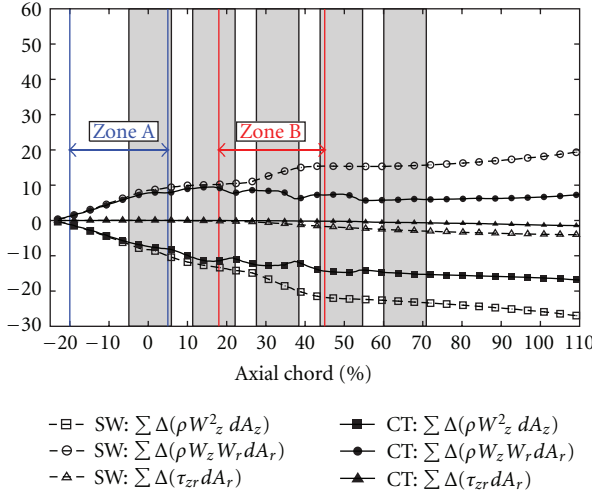


FIGURE 16: NASA Rotor 37 with and without CT: cumulative sum in the axial direction of the principal terms involved in the axial momentum equation.

unsteadiness of blade passage is weak. One reason to this phenomena might come from the ratio between the slot area and the area between the individual slots (which is very small here). Despite the high temporal resolution of the CT slot passing temporal period ($T_{CT} = 170$ iterations), this particular test case fails to meet expectations in terms of analysis of unsteady flow interaction between the CT slots and the rotor channel. However, the effort is now focused on the analysis of local changes of the axial momentum balance in order to get more qualitative and quantitative information on the contribution of the CT slots.

6.4. Longitudinal Evolutions of the Axial Forces and CT Contribution. Since axial forces due to $-\sum \Delta(\tau_{rz} A_r)$, $\sum \Delta(\rho W_z W_r A_r)$, and $\sum \Delta(\rho W_z^2 A_z)$ highlight the change between SW and CT cases, it is interesting to investigate their respective axial evolution to further understand the flow interaction between CT and the throughflow. Figures 16 and 18 present the cumulative sum along the axial direction of these terms, respectively, for the NASA Rotor 37 and CBUAA. Figure 17 recalled from Legras et al. [37] the cumulative sum for the CREATE compressor of both steady and unsteady axial momentum balances. In the current study, only the unsteady curves are analyzed. Further comments on the difference between the steady and unsteady results are discussed in Legras et al. [37]. These diagrams provide information on the region where flow is highly constrained and on individual grooves contribution. The shaded bands denote the axial location of the casing grooves.

6.4.1. SW Results. Results of all SW configurations show that the efforts evolve in amplitude in a nonlinear manner along the axial direction.

The curve of viscous term $-\Delta(\tau_{rz} A_r)$ begins to grow near the leading edge. To relate these trends to the flow physics, Figure 19(a) presents at the mid-height of the CBUAA rotor tip gap, the flow field of $-\Delta(\tau_{rz} A_r)$. It can be observed that the growth of $-\Delta(\tau_{rz} A_r)$ can be relied firstly to the tip leakage vortex (referred as region A in Figure 19(a)) and secondly to the interaction of the detached shock with the shroud boundary layers (in a less pronounced manner).

Concerning the curve of the term $\Delta(\rho W_z^2 A_z)$, it begins to grow in negative value before the blade leading edge for the NASA Rotor 37 and CBUAA cases. Contour plots of $\Delta(\rho W_z^2 A_z)$ in the CBUAA rotor tip gap presented. Figure 20(a) reveals that this growing trend is linked to the flow acceleration before the blade detached shock. Next, the curve slightly increases in positive values. This observation relates to the incoming flow deceleration due to its interaction with the tip leakage flow. Further downstream in the blade channel, the curve increases in negative values due to the presence of the tip leakage flow.

The curve of term $\Delta(\rho W_z W_r A_r)$ axially evolves in “quasi-” opposite magnitude of $\Delta(\rho W_z^2 A_z)$ curve. In fact, W_r acts here as a “coefficient of amplification.” This observation is confirmed by Figure 21(a), where contour plots are very similar to those of $\Delta(\rho W_z^2 A_z)$ in Figure 20(a).

To resume, the SW results highlight strong axial force magnitude due to the tip leakage flow and, when a detached blade shock exists, due to the interaction between leakage flow and blade passage shock. However, the detached blade shock has a lower influence in term of force magnitude than the tip leakage flow. It explains why the axial momentum balances of CREATE (subsonic regime) and CBUAA (transonic regime) are very similar. Concerning the difference of $\Delta(\rho W_z W_r A_r)$ and $\Delta(\rho W_z^2 A_z)$ between NASA Rotor 37 and CBUAA, it can clearly be explained by the casing shape. In fact, the rapid growth of $\Delta(\rho W_z W_r A_r)$ and $\Delta(\rho W_z^2 A_z)$ curves in NASA Rotor 37 corresponds to the location of the greatest slope of the casing form.

6.4.2. CT Results. Results of the CT configurations clearly highlight the local contribution of the slots.

For both axi- and non-axisymmetric CT, the curve shapes of the viscous term $-\Delta(\tau_{rz} A_r)$ are very similar to those of the SW cases, except that CT delays further downstream the beginning of the growth rate. Since this term can be relied to the tip leakage flow, this observation can be explained by an attenuation of the spread of the leakage flow perpendicular to the blade. This is confirmed when comparing Figures 19(a) and 19(b). Moreover, referring to the CBUAA histograms in Figure 13, CT configuration shows higher magnitude of viscous term $-\Delta(\tau_{rz} A_r)$. In fact, contour plots in Figure 19(b) indicate the presence of a second region of high viscous axial force denoted B and located along the rear part of the CT slots. As seen by Legras et al. [44], this part of the slot is responsible for flow bleeding, whereas at the front part the recirculated flow is reinjected into the throughflow. This observation suggests that the flow bleeding mechanism induces strong shear layer that can

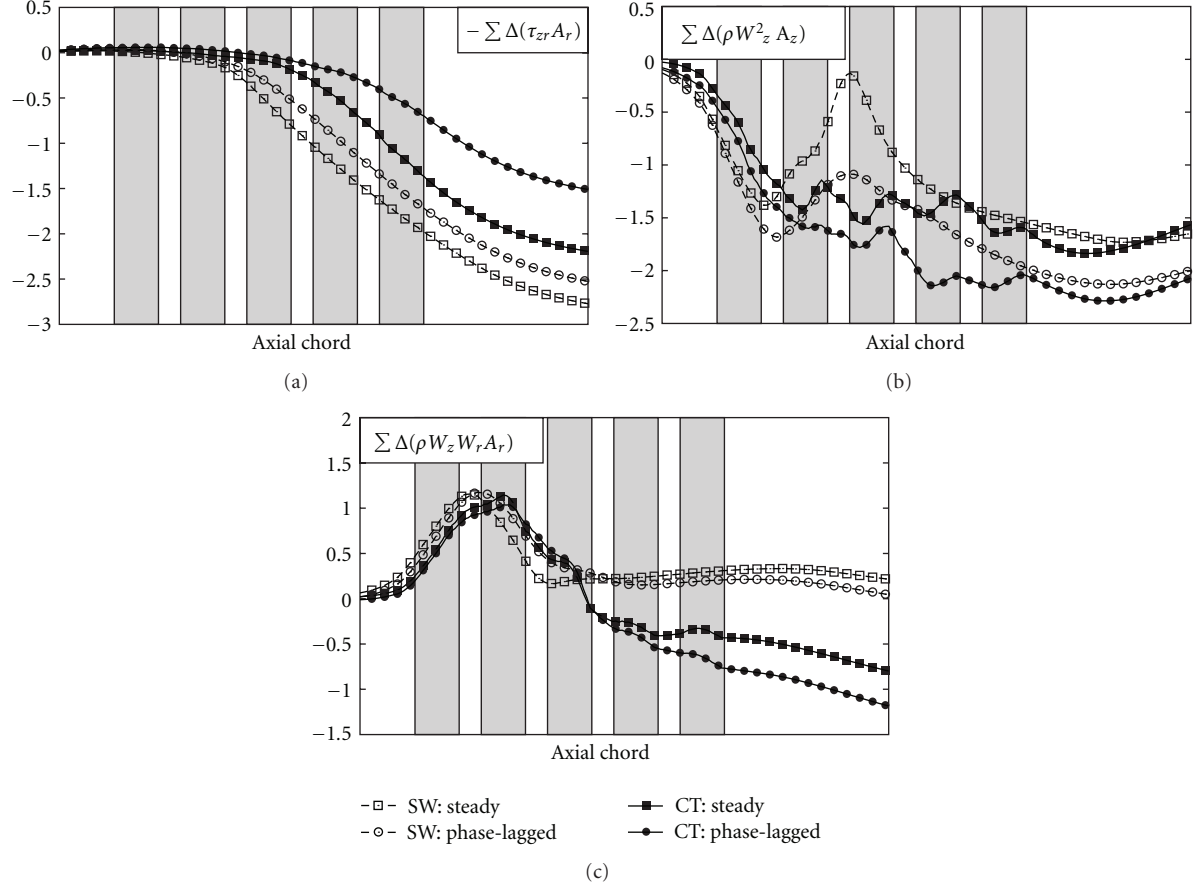


FIGURE 17: CREATE-R2 with and without CT: cumulative sum in the axial direction of the principal terms involved in the axial momentum equation [37].

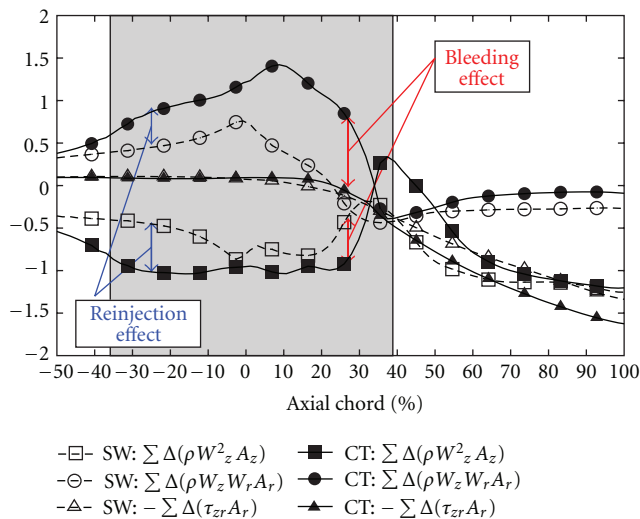
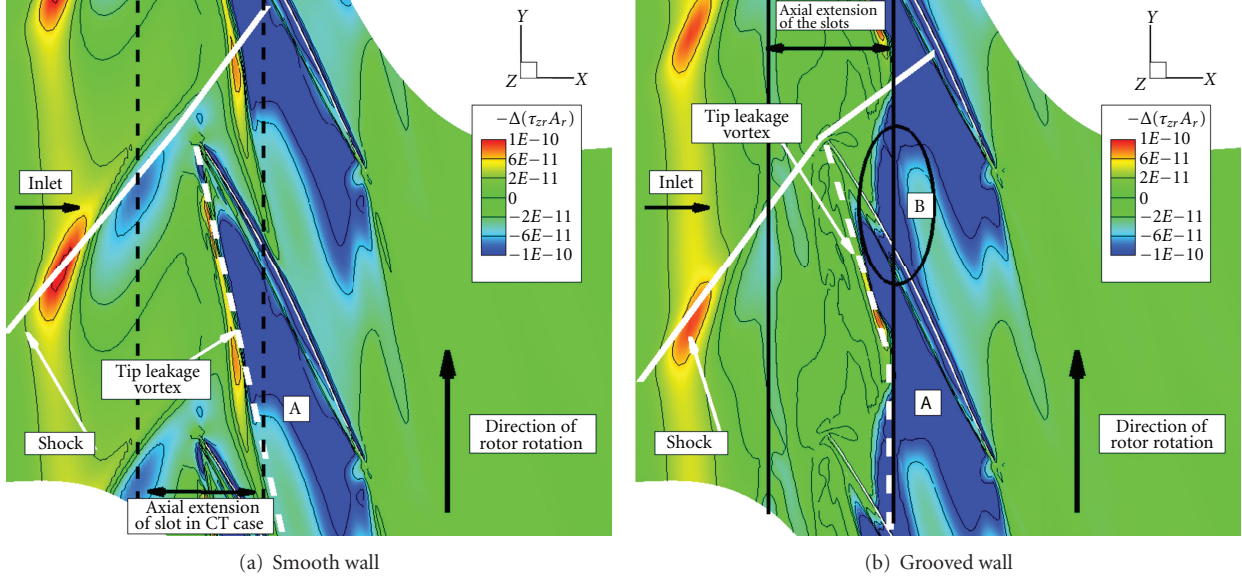
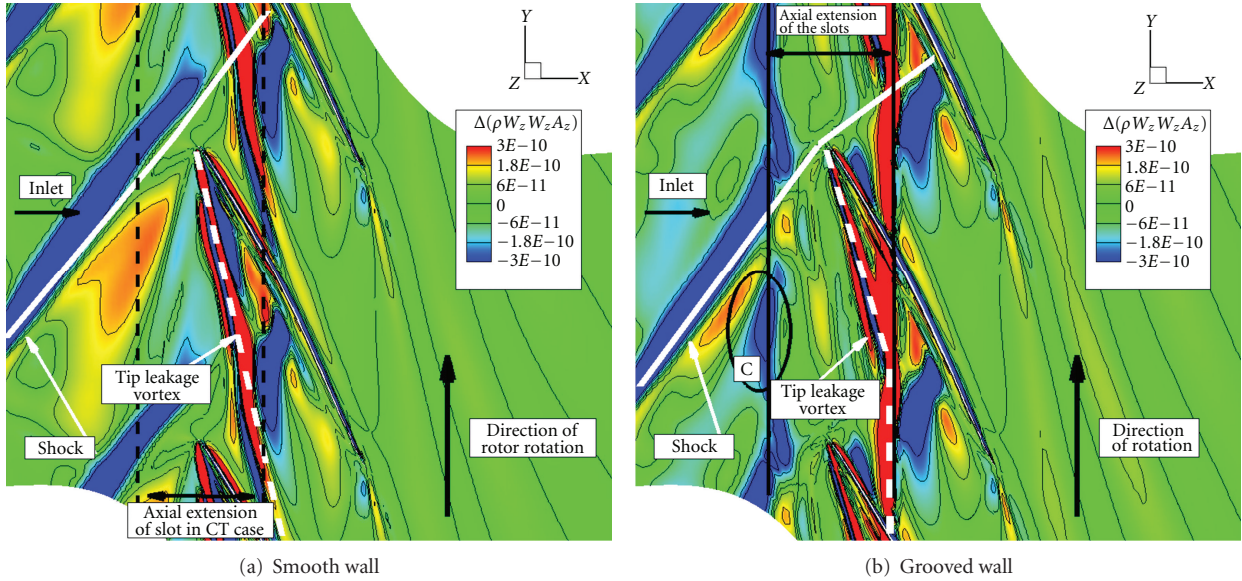


FIGURE 18: CBUAA with and without CT: cumulative sum in the axial direction of the principal terms involved in the axial momentum equation.

increase viscous losses, thus explaining the efficiency losses observed with the use of the slot-type CT.

The CT effects are even more highlighted by the curve of $\Delta(\rho W_z W_r A_r)$. In fact, one can notice that axisymmetric CTs in NASA Rotor 37 and CREATE cases create an axial force $\Delta(\rho W_z W_r A_r) < 0$ in opposite direction to the flow advance. This explains the change observed in the previous histograms (Figures 11 and 12). This creation of axial force $\Delta(\rho W_z W_r A_r) < 0$ can be relied to the bleeding effect of the grooves since $W_r > 0$ has been observed in previous studies [9, 37]. Moreover, this kind of analysis permits to identify the groove effectiveness depending on its capability to create this previous axial force, thus a bleeding effect. For the NASA Rotor 37, results show that the 2nd, 3rd, and 4th grooves are useful at the last stable point numerically seen for SW configuration. For the CREATE, Legras et al. [37] conclude that the 3rd groove is efficient at the last stable point numerically seen for SW configuration.

Concerning the CBUAA slot-type CT, the bleeding effect along the rear part of the CT slots creates an axial force $\sum \Delta(\rho W_z W_r A_r) < 0$ directed along the flow advance. This observation is confirmed by Figure 21(a) and is referred as

FIGURE 19: CBUAA: Flow field denoted at midgap by negative values of $-\Delta(\tau_{zr} A_r)$.FIGURE 20: CBUAA: Flow field denoted at midgap by negative values of $\Delta(\rho W_z^2 A_z)$.

zone D. As a matter of fact, the bleeding mechanisms of slot-type CT have a relatively similar effect than observed with circumferential CT. This is consistent with the general conclusions that previous studies have found that the reverse tip leakage flow through the tip gap got pushed into the grooves by the reinjecting flow (in main flow direction) from the grooves. On the contrary, the flow blowing mechanism along the front part of the CT induces axial force of $\sum \Delta(\rho W_z W_r A_r) > 0$ acting in opposite direction to the flow advance (referred as zone C in Figure 21(a)). In fact, the reinjected flow tends to radially deviate the incoming flow.

Concerning the term of $\Delta(\rho W_z^2 A_z)$, curves mainly evolve in opposite magnitude to the term $\sum \Delta(\rho W_z W_r A_r)$. Moreover, results of CBUAA with slot-type CT indicate that the blowing mechanism at the CT front part creates an axial force $\Delta(\rho W_z^2 A_z) < 0$ in the direction to the flow advance (see Figure 20(b), zone C). This observation suggests that the near casing flow is further accelerated. This is consistent with previous studies that the reinjected flow energizes the near casing flow. On the contrary, the flow bleeding mechanism creates an axial force $\Delta(\rho W_z^2 A_z) > 0$ in the opposite direction to the flow advance. This is consistent since the near

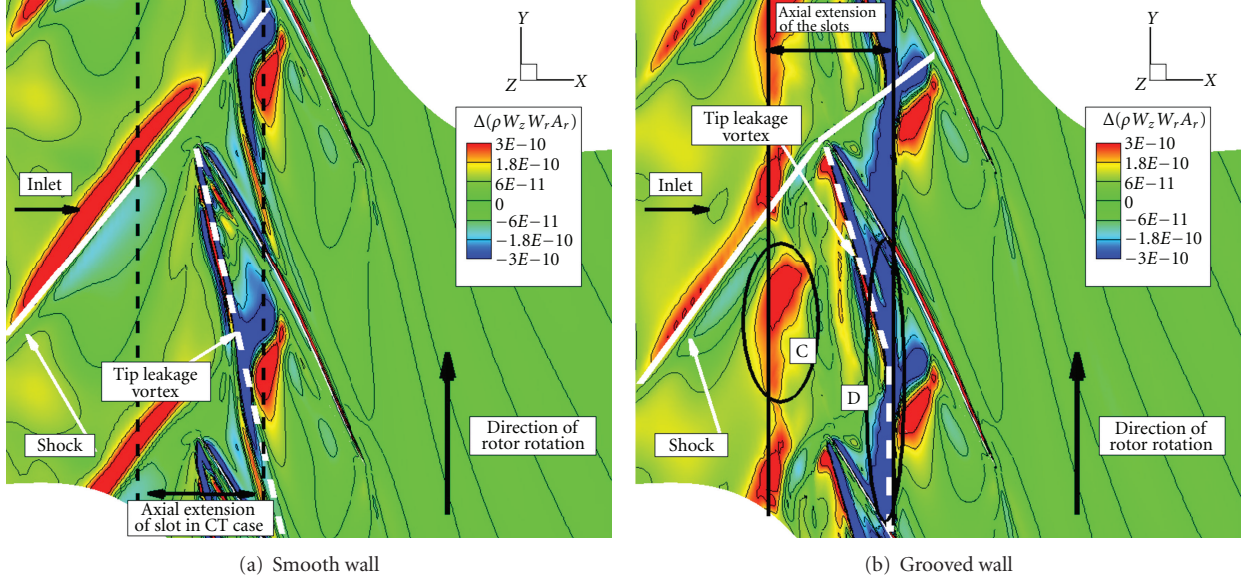


FIGURE 21: CBUAA: Flow field denoted at midgap by negative values of $\Delta(\rho W_z W_r A_r)$.

casing flow bled lost its axial velocity in order to be radially deflected into the CT slots.

6.5. Recommendation on the Useful Interpretation of the CT Flow Mechanisms Using the ESA Model. The analysis of the slot-type CT of the CBUAA compressor shows the limitation of the use of the histograms as a tool to investigate CT flow mechanisms. In fact, the histograms present a global overview of the forces being applied on a rotor tip control volume. They tend to “smooth” the local effect of CT flow mechanisms (mainly both bleeding and blowing mechanisms). For an analysis of axisymmetric CT, histograms can be useful, whereas for slot-type CT the histograms prove to be not sufficient. Thus, one has to take care of the interpretation of the histograms. The main interest of the model comes from the analysis of the longitudinal evolutions of the axial forces since it permits to reveal the local CT flow mechanisms as well as the CT individual grooves’ contribution. So, it is recommended to perform both global and local analysis using the ESA model in order to further understand the flow mechanisms induced by CT.

7. Conclusion

This paper has presented a generalized method of the Shabbir and Adamczyk approach for uncovering the flow mechanisms induced by casing treatment (CT) using CFD numerical simulations. Compared to Shabbir’s approach, this method permits to analyze any CT geometry, thanks to a budget analysis of each of the Navier-Stokes (un)steady momentum equations. In the current paper, only the equilibrium of the axial momentum equations is analyzed since it describes the global flow across the rotor channel, specially its

pressure rise. The novel method has been used to investigate the flow interaction between axi and non-axisymmetric CT and the throughflow for three different axial compressors. They differ by the flow regime (subsonic/transonic), the untreated casing shape (cylindrical/conical), and the CT implemented (axi-/non axisymmetric CT).

The comparison of the three compressors indicates that axisymmetric CT is characterized by its flow bleeding effect that creates an axial force $\Delta(\rho W_z W_r A_r) < 0$. It is shown that the benefit of this force on the flow stability is more dependant on the casing shape than the flow regime. Concerning slot-type CT, it is characterized by both a bleeding effect at the rear part, which creates an axial force $\Delta(\rho W_z W_r A_r) < 0$, and a blowing effect at the front part that energizes the near casing flow by creating axial force $\Delta(\rho W_z^2 A_z) < 0$. However, its strong bleeding effect is responsible of additional viscous losses explaining the efficiency losses observed with the use of slot-type CT. These conclusions are rather difficult to be stated from the only histograms. Thus, it is strongly recommended to focus on the axial distribution of the axial forces to further understand the interaction between the CT and the flow. Furthermore, since both axi- and non-axisymmetric CT create an axial force $\Delta(\rho W_z W_r A_r) < 0$, it lends support that the radial velocity component W_r is of a main interest for the stability of the tip flow.

The current analysis methodology proved its potential to help in the designing of CT. However, there are still many questions on the understanding of the CT mechanisms that the model can answer. The main perspectives concern

- (i) the analysis of tangential momentum: since the tangential force is the main force of compressors, it could be interesting to investigate the influence of CT,

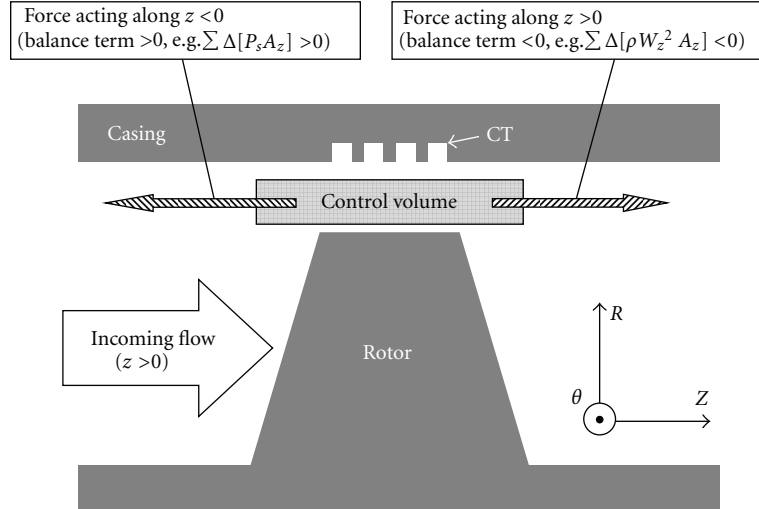


FIGURE 22: Nomenclature and sketch of the axial forces acting on a control volume located in the rotor tip clearance.

- (ii) the analysis of the balance at part speed,
- (iii) the resolution of the momentum equation in the streamline reference frame rather than cylindrical.

Finally, it can also be easily used to uncover the flow mechanisms in order to design a large panel of flow passive control devices: film cooling, and boundary layer aspiration in the turbomachinery field as well as for aircraft or helicopter applications.

Nomenclature

Symbols

- A: Surface area of a grid cell = $[A_r, A_\theta, A_z]^T$
 E_r : Relative energy
 F_{cen} : Centrifugal force
 F_{cor} : Coriolis force
 $F_{\lambda_{2,4}}$: 2nd- and 4th-order numerical scalar artificial dissipation fluxes
 \dot{m} : Mass flow rate
 P_s : Static pressure
 \mathbf{q} : Heat flux vector = $[q_r, q_\theta, q_z]^T$
Q: Conservative variable
R: Numerical modelling residual
R: Number of rotor row
Rpi: Total-to-total pressure ratio
 r, θ, z : Cylindrical coordinates
S: Number of stator row
t: Time

- V: Volume of the control domain
 \mathbf{V} : Absolute velocity = $[V_r, V_\theta, V_z]^T$
 \mathbf{W} : Relative velocity = $[W_r, W_\theta, W_z]^T$.

Greek Letters

- η_{is} : Isentropic efficiency
 γ : Specific heat ratio
 μ : Molecular dynamic viscosity
 ω : Rotation speed
 ρ : Density
 τ : Sum of the viscous and turbulence stress tensor.

Abbreviation

- CBUAA: Compressor of the Beijing University of Aeronautics & Astronautics
CT: Casing treatment
ESA: Extended Shabir and Adamczyk model
SW: Smooth wall.

Acknowledgments

The authors are grateful to Snecma, SAFRAN Group, for permission to publish results. Special thanks to LMFA and the CERFACS-CFD team for their computational facilities as well as for their availability for discussions concerning numerical methods and physical analysis. The authors are also grateful to the *elsA* software team (ONERA).

References

- [1] E. M. Greitzer, J. P. Nikkanen, D. E. Haddad, R. S. Mazzawy, and H. D. Joslyn, "Fundamental criterion for the application of rotor casing treatment," *Journal of Fluids Engineering*, vol. 101, no. 2, pp. 237–243, 1979.
- [2] D. C. Rabe and C. Hah, "Application of casing circumferential grooves for improved stall margin in a transonic axial compressor," in *Proceedings of the ASME Turbo Expo: Turbomachinery*, paper GT2002-30641, pp. 1141–1153, June 2002.
- [3] A. Shabbir and J. J. Adamczyk, "Flow mechanism for stall margin improvement due to circumferential casing grooves on axial compressors," *Journal of Turbomachinery*, vol. 127, no. 4, pp. 708–717, 2005.
- [4] V. Perrot, A. Touyeras, and G. Lucien, "Detailed cfd analysis of a grooved casing treatment on an axial subsonic compressor," in *Proceedings of the 7th European Turbomachinery Conference*, 2007.
- [5] M. W. Müller, H. P. Schiffer, and C. Hah, "Effect of circumferential grooves on the aerodynamic performance of an axial single-stage transonic compressor," in *Proceedings of the ASME Turbo Expo*, paper GT2007-27365, pp. 115–124, May 2007.
- [6] M. W. Müller, C. Biela, and H. P. Schiffer, "Interaction of rotor and casing treatment flow in an axial single-stage transonic compressor with circumferential grooves," in *Proceedings of the ASME Turbo Expo*, paper GT2008-50135, pp. 67–78, June 2008.
- [7] T. Houghton and I. Day, "Enhancing the stability of subsonic compressors using casing grooves," in *Proceedings of the ASME Turbo Expo*, paper GT2009-59210, pp. 39–48, June 2009.
- [8] G. Legras, N. Gourdain, and I. Trébinjac, "Numerical analysis of the tip leakage flow field in a transonic axial compressor with circumferential casing treatment," *Journal of Thermal Science*, vol. 19, no. 3, pp. 198–205, 2010.
- [9] G. Legras, N. Gourdain, and I. Trébinjac, "Extended methodology for analysing the flow mechanisms induced by casing treatment in compressor," in *Proceedings of the 9th of European Turbomachinery Conference*, 2011.
- [10] I. Wilke and H. P. Kau, "A numerical investigation of the flow mechanisms in a high pressure compressor front stage with axial slots," *Journal of Turbomachinery*, vol. 126, no. 3, pp. 339–349, 2004.
- [11] I. Wilke, H. P. Kau, and G. Brignole, "Numerically aided design of a high-efficient casing treatment for a transonic compressor," in *Proceedings of the ASME Turbo Expo*, paper GT2005-68993, pp. 353–364, Reno, Nev, USA, June 2005.
- [12] N. Gourdain and F. Leboeuf, "Unsteady simulation of an axial compressor stage with casing and blade passive treatments," *Journal of Turbomachinery*, vol. 131, no. 2, pp. 1–12, 2009.
- [13] M. Vogues, R. Schnell, C. Willert, R. Monig, M. W. Muller, and C. Zschep, "Investigation of blade tip interaction with casing treatment in a transonic compressor. Part 1: Particle image velocimetry," *ASME Journal of Turbomachinery*, vol. 133, no. 1, Article ID 011007, 2011.
- [14] R. Schnell, M. Voges, R. Mönig, M. W. Müller, and C. Zschep, "Investigation of blade tip interaction with casing treatment in a transonic compressor-part II: numerical results," *Journal of Turbomachinery*, vol. 133, no. 1, Article ID 011008, 2011.
- [15] M. D. Hathaway, "Self-recirculating casing treatment concept for enhanced compressor performance," in *Proceedings of the ASME Turbo Expo: Turbomachinery*, paper GT-2002-30368, pp. 411–420, June 2002.
- [16] H. Yang, D. Nuernberger, E. Nicke, and A. Weber, "Numerical Investigation of Casing Treatment Mechanisms with a Conservative Mixed-Cell Approach," in *ASME Turbo Expo*, paper GT2003-38483, pp. 961–974, June 2003.
- [17] A. J. Strazisar, M. M. Bright, S. Thorp, D. E. Culley, and K. L. Suder, "Compressor stall control through endwall recirculation," in *Proceedings of the ASME Turbo Expo*, paper GT2004-54295, pp. 655–667, June 2004.
- [18] N. Gourdain, X. Ottavy, and F. Wlassow, "Effect of Tip Clearance Dimensions and Control of Unsteady Flows in a Multi-Stage High Pressure Compressor," *Journal of Turbomachinery*. In press.
- [19] M. D. Hathaway, "Passive endwall treatments for enhancing stability," VKI LS 2006-06 on Advances in Axial Compressor Aerodynamics, 2007.
- [20] J. Dunham, "CFD validation for propulsion system components (la validation CFD des organes des propulseurs)," Tech. Rep. number ISBN 92-836-1075-X, AGARD Advisory Report 355, 1998.
- [21] A. Jameson, R. F. Schmidt, and E. Turkel, "Numerical Solutions of the Euler equations by finite volume methods using Runge-Kutta time stepping," AIAA paper AIAA-81-1259, 1981.
- [22] F. Lin, F. Ning, and H. Liu, "Aerodynamics of compressor casing treatment part I: experiment and time-accurate numerical simulation," in *Proceedings of the ASME Turbo Expo*, paper GT2008-51541, pp. 731–743, June 2008.
- [23] J. Ratzlaff, P. D. Orkwis, C. Noll, and G. Steuber, "Analysis of lumped deterministic source terms and their sub-components in a stage 1 high pressure turbine rotor," in *Proceedings of the ASME Turbo Expo*, paper GT2008-51473, pp. 2693–2703, June 2008.
- [24] L. Reid and R. Moore, "Design and overall performance of four highly loaded high-speed inlet stages for 19 an advanced high pressure ratio core compressor," Tech. Rep. TP 1337, NASA Lewis Research Center, 1978.
- [25] R. D. Moore and L. Reid, "Performance of single-stage axial-flow transonic compressor with rotor and stator aspect ratios of 1.19 and 1.26, respectively, and with design pressure ratio of 2.05," *NASA Technical Paper*, no. 1659, 1980.
- [26] A. Touyeras and M. Villain, "Aerodynamic design and test result analysis of a three stage research compressor," in *Proceedings of the ASME Turbo Expo*, paper GT2004-53940, pp. 589–597, June 2004.
- [27] F. Ning and L. Xu, "Aerodynamics of compressor casing treatment Part II: a quasi-steady model for casing treatment flows," in *Proceedings of the ASME Turbo Expo*, paper GT2008-51542, pp. 745–755, June 2008.
- [28] K. L. Suder and M. L. Celestina, "Experimental and computational investigation of the tip clearance flow in a transonic axial compressor rotor," *Journal of Turbomachinery*, vol. 118, no. 2, pp. 218–229, 1996.
- [29] R. V. Chima, "Calculation of tip clearance effects in a transonic compressor rotor," *Journal of Turbomachinery*, vol. 120, no. 1, pp. 131–140, 1998.
- [30] J. D. Denton, "Lessons from rotor 37," in *Proceedings of the 3rd International Symposium on Experimental and Computational Aerothermodynamics of Internal Flows (ISAIF'96)*, 1996.
- [31] Wilke I., *Verdichterstabilisierung mit passiven Gehäusestrukturen—eine numerische analyse*, Ph.D. thesis, Technischen Universität München, 2005.
- [32] D. Arnaud, X. Ottavy, and A. Vouillarmet, "Experimental investigation of the rotor-stator interactions, within a high speed, multi-stage, axial compressor part 1—Experimental

- facilities and results,” in *Proceedings of the ASME Turbo Expo*, paper GT2004-53764, pp. 903–914, June 2004.
- [33] D. Arnaud, X. Ottavy, and A. Vouillarmet, “Experimental investigation of the rotor-stator interactions within a high-speed, multi-stage, axial compressor. Part 2. Modal analysis of the interactions,” in *2004 ASME Turbo Expo*, pp. 915–924, aut, June 2004.
 - [34] V. Sharma, M. Schvallinger, J. Marty et al., “Turbulence modelling effects on off-design predictions for a multistage compressor,” in *Proceedings of the 18th International Symposium on Air Breathing Engines (ISABE'07)*, p. 1183, 2007.
 - [35] J. Marty, G. Cottin, and B. Aupoix, “Turbulence modelling and transition to turbulence effects for a high pressure multistage compression,” in *Proceedings of the 8th European Turbomachinery Conference*, 2009.
 - [36] N. Gourdain, X. Ottavy, and A. Vouillarmet, “Experimental and numerical investigation of unsteady flows in a high speed three stages compressor,” in *Proceedings of the 8th European Turbomachinery Conference*, 2009.
 - [37] G. Legras, N. Gourdain, I. Trébinjac, and X. Ottavy, “Analysis of Unsteadiness on Casing Treatment Mechanisms in an Axial Compressor,” in *Proceedings of the ASME Turbo Expo*, ASME paper GT2011-46806, 2011.
 - [38] L. Cambier and J. P. Veuillot, “Status of the elsA CFD software for flow simulation and multidisciplinary applications,” in *Proceedings of the 46th AIAA Aerospace Sciences Meeting and Exhibit*, January 2008.
 - [39] L. Castillon, S. Péron, and C. Benoit, “Numerical simulations of technological effects encountered on turbomachinery configurations with the chimera technique,” in *Proceedings of the 27th Congress of the International Council of the Aeronautical Sciences (ICAS'10)*, paper 088, 2010.
 - [40] J. I. Erdos, E. Alzner, and W. McNally, “Numerical solution of periodic transonic flow through a fan stage,” *AIAA Journal*, vol. 15, no. 11, pp. 1559–1568, 1977.
 - [41] G. A. Gerolymos, G. J. Michon, and J. Neubauer, “Analysis and application of chorochronic periodicity in turbomachinery rotor/stator interaction computations,” *Journal of Propulsion and Power*, vol. 18, no. 6, pp. 1139–1152, 2002.
 - [42] L. Castillon and G. Legras, “An unsteady overset grid method for the simulation of compressors with non circumferential casing treatments,” in *Proceedings of the 20th International Symposium on Air Breathing Engines (ISABE'11)*, 2011.
 - [43] D. C. Wilcox, “Reassessment of the scale-determining equation for advanced turbulence models,” *AIAA Journal*, vol. 26, no. 11, pp. 1299–1310, 1988.
 - [44] G. Legras, L. Castillon, I. Trébinjac, and N. Gourdain, “Flow mechanisms induced by non-axisymmetric casing treatment in a transonic axial compressor,” in *Proceedings of the 10th International Symposium on Experimental and Computational Aerothermodynamics of Internal Flows (ISAIF'11)*, 2011.
 - [45] B. H. Beheshti, J. A. Teixeira, P. C. Ivey, K. Ghorbanian, and B. Farhanieh, “Parametric study of tip clearance—casing treatment on performance and stability of a transonic axial compressor,” *Journal of Turbomachinery*, vol. 126, no. 4, pp. 527–535, 2004.
 - [46] C. Haixin, F. Song, and X. Huang, “CFD Investigation on Tip Leakage Flow and Casing Treatment of a Transonic Compressor,” in *Proceedings of the 17th International Symposium on Air Breathing Engine*, 2005.
 - [47] H. Xudong, C. Haixin, and F. Song, “CFD Investigation on the circumferential grooves casing treatment of transonic compressor,” in *Proceedings of the ASME Turbo Expo*, paper GT2008-51107, pp. 581–588, June 2008.

